Acta Crystallographica Section A
Foundations of Crystallography
ISSN 0108-7673

Received 14 July 2000
Accepted 24 November 2000

Generalized extinction in bipyramidal crystals

G. Thorkildsen,[a]* H. B. Larsen,[b] D. Semmingsen[c] and Ø. Bjaanes[b]

[a]Department of Mathematics and Natural Science, Stavanger University College, Ullandhaug, N-4091 Stavanger, Norway, [b]Department of Materials Science, Stavanger University College, Ullandhaug, N-4091 Stavanger, Norway, and [c]Department of Agriculture and Science, Hedmark University College, N-2322 Ridabu, Norway. Correspondence e-mail: gunnar.thorkildsen@tn.his.no

The generalized extinction factors for a set of strong reflections as a function of wavelength are obtained by indirect measurements. The experiments are performed on a crystalline system that satisfies the geometrical requirements imposed by theoretical models developed for a finite perfect crystal. With increased perfection, represented by a reduction in the width of the mosaic distribution function from three to one thousandth of a degree, the experiments give results that approach the predictions from the theory. The present procedure utilizes measurements of the integrated diffracted power of a weak reflection for scaling the strong reflections, hence non-measurable wavelength-dependent factors are assumed to be eliminated.

1. Introduction

One inherent difficulty in accurate structure determination studies is to obtain reliable estimates of the extinction effects. That is the reduction of intensity owing to either coherently or incoherently multiply scattered waves (primary and secondary extinction, respectively). *A priori* determination of such effects is rarely carried out. The standard procedure is to calculate extinction parameters from the least-squares structure-refinement procedure (Zachariasen, 1967; Becker & Coppens, 1974*a*,*b*, 1975).

As shown in previous theoretical works (Thorkildsen & Larsen, 1998*a*,*b*,*c*, 1999*a*), the *generalized extinction factor*, that is the combined influence of primary extinction and ordinary absorption, strongly depends upon the crystal shape and the scattering geometry. The basis for the analysis has been the Takagi–Taupin equations (Takagi, 1962, 1969; Taupin, 1964), which are formulated in the case of a finite perfect crystal and solved with appropriate boundary conditions.

The perfect crystal gives rise to extreme multiple-scattering effects, *i.e.* it represents the case of minimum value for the generalized extinction factor. Thus, if we want to assess the influence of crystal imperfections on the scattering processes, it is important to have reliable estimates of this perfect-crystal limit.

In this work, we demonstrate the calculation and measurement of the generalized extinction factor for nearly perfect bipyramidal crystals at different wavelengths. For proper comparison, the theoretical basis is extended to cover all actual scattering situations. The theoretical development is given in §2. This also includes the calculation of rocking curves. The experimentally generalized extinction factors cannot be reliably deduced unless careful measurements of rocking curves are performed, in our case by appropriate ω scans. The experiments are presented in §3, while the method of analysis, the results and discussion are covered in §§4–5. The final conclusions are given in §6. Some mathematical details are postponed to Appendices.

The wavelength dependence of extinction has been frequently studied in the past three decades, mainly aiming at testing different theories used in the refinements (Niimura *et al.*, 1975; Cooper & Rouse, 1976; Cooper, 1979; Palmer & Jauch, 1995) or extracting 'extinction-free' structure factors by extrapolation to zero wavelength (Mathieson, 1977, 1979; Hester & Okamura, 1996; Graafsma *et al.*, 1998; Lippmann & Schneider, 2000). A different approach was applied by Stevenson & Barnea (1983) who considered extinction-related differences in the Bijvoet ratios of zinc selenide (ZnSe). Suortti (1982*a*,*b*) also devised a method for experimental correction for primary and secondary extinction. The application of γ diffractometry to the problem has been discussed by Schneider (1977).

2. Theory

In TL98*c* (Thorkildsen & Larsen, 1998*c*), TL99*a* (Thorkildsen & Larsen, 1999*a*) and TL99*b* (Thorkildsen & Larsen, 1999*b*), the procedures for calculating generalized extinction factors, ordinary absorption factors and rocking curves were outlined for perfect crystals having a rectangular $t \times l$ cross section. The results were all derived from the Takagi–Taupin equations using the point-source concept and the Riemann–Green method.

Those works were however limited to the *AB–AD* scattering configuration, *cf.* Fig. 1(*a*), having[1] $0 \le \theta_{oh} \le (\pi/4)$ and $-\theta_{oh} \le \gamma \le \theta_{oh}$. Another scattering configuration, *AB–CD* scattering, *cf.* Fig. 1(*b*), is realised when $0 \le \theta_{oh} \le (\pi/4)$ and $\theta_{oh} \le \gamma \le (\pi/2) - \theta_{oh}$. θ_{oh} is the Bragg angle and γ is the angle between the inward drawn normal to the surface B and the trace of the reflecting lattice planes. These two cases together cover all possible (with appropriate interchange of t and l) low-angle scattering situations. The latter case, *AB–CD* scattering, is even easier to handle than the former, since only a single region m is formed within the crystal by the ray-tracing procedure shown in Figs. 3 and 4 of TL98*c*. This situation may be classified as a case of 'pure' *Laue* scattering and the extended volume emerging from the surface integration set-up equals the true volume of the crystal, *cf.* Becker & Dunstetter (1984).

The generalized extinction factor, y, for the *AB–CD* scattering geometry may be expressed by

$$y = \mathcal{N}_y \sum_{j=C,D} \sum_{i=A,B} \int_{M_{i-j}(\zeta)} \mathrm{d}y \int_{S_{i-j}(y,\zeta)} \mathrm{d}x \times \left| G_h^{i-j}(u|x,y) A_h^{i-j}(\mu_0|x,y) \right|^2, \quad (1)$$

while the corresponding expression for the intrinsic power, *cf.* equation (10) of TL99*b*, becomes

$$P_h^{(0)}(\Delta\theta_{oh}) = \mathcal{N}_p \sum_{j=C,D} \int_{M_j(\zeta)} \mathrm{d}y \left| \sum_{i=A,B} \int_{S_{i-j}(y,\zeta)} \mathrm{d}x\, G_h^{i-j}(u|x,y) \times Q_h^{i-j}(\xi_0, \Delta\theta_{oh}, \Delta\theta_{oh}^0|x,y) A_h^{i-j}(\mu_0|x,y) \right|^2. \quad (2)$$

The coupled surface integrations are expressed in dimensionless variables x and y, spanning the entrance and exit surfaces, respectively. The explicit expressions for the Green functions, G_h^{i-j}, the phase factors, Q_h^{i-j}, and the factors A_h^{i-j} related to ordinary absorption, as well as the parameters ζ, u, ξ_0, $\Delta\theta_{oh}^0$ and μ_0 are given in Appendix *A*. ζ and ξ_0 are purely geometrical quantities. u is inversely proportional to the square of the extinction length and is thus a measure of the scattering power. μ_0 is proportional to the linear absorption coefficient. All these parameters appear in the formalism as dimensionless numbers. $\Delta\theta_{oh}^0$ determines the deviation from the kinematical Bragg angle caused by refraction due to the average polarizability of the crystal.

The actual integration set-up, $\{\int_{M_{i-j}(\zeta)}, \int_{S_{i-j}(y,\zeta)}\}$, is summarized in Appendix *B*. In this work, the intrinsic power is normalized to give the generalized extinction factor when integrated across the deviation from the Bragg condition, $\Delta\theta_{oh}$,

$$y = \int_{-\infty}^{+\infty} P_h^{(0)}(\Delta\theta_{oh})\, \mathrm{d}\Delta\theta_{oh}. \quad (3)$$

The normalizing constants $\mathcal{N}_y$ and $\mathcal{N}_p$ are given by

$$\mathcal{N}_y = 1/2\zeta, \quad \mathcal{N}_p = \xi_0/4\zeta.$$

[1] This scattering scheme is also realised for $(\pi/4) \le \theta_{oh} \le (\pi/2)$ and $\theta_{oh} - (\pi/2) \le \gamma \le (\pi/2) - \theta_{oh}$.

The formulas may be extended to cover crystals having cross sections that vary along the direction perpendicular to the plane of diffraction: $t \times l \rightarrow t(z) \times l(z)$, *cf.* Fig. 2. By introduction of the dimensionless coordinate w by $z = wh$, where h is the height of the crystal above its base plane, the parameters of the calculation are rescaled according to

$$\begin{aligned} u &\rightarrow u(w) = u(0)(1 - ws)^2 \\ \mu_0 &\rightarrow \mu_0(w) = \mu_0(0)(1 - ws) \\ \xi_0 &\rightarrow \xi_0(w) = \xi_0(0)(1 - ws) \\ \zeta &\rightarrow \zeta(w) = \zeta(0)(1 - wr)/(1 - ws), \end{aligned}$$

with $s = [l(0) - l(h)]/l(0)$ and $r = [t(0) - t(h)]/t(0)$. The expressions for the generalized extinction factor and the intrinsic power then become

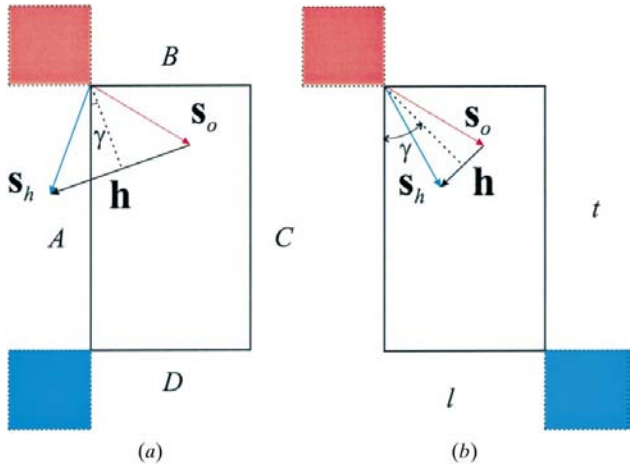

Figure 1
The actual scattering situations: (*a*) $AB - AD$ scattering and (*b*) $AB - CD$ scattering. In both cases, the crystal surfaces A and B constitute the entrance surface, *i.e.* the direction of the unit vector $\mathbf{s}_o$, parallel to the wavevector of the incident beam, is confined to the sector marked by the red square. The surfaces (*a*) A and D or (*b*) C and D constitute the exit surface in the two cases. Thus the direction of the unit vector $\mathbf{s}_h$, parallel to the wavevector of the diffracted beam, is confined to the sector marked by a blue square.

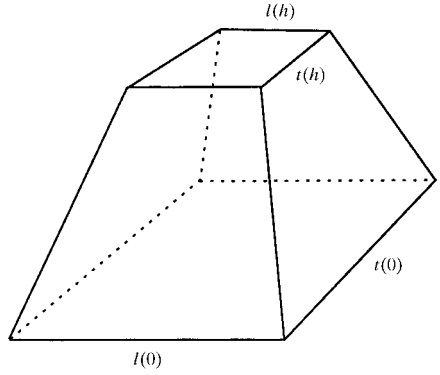

Figure 2
Basic crystal shape, described by the symmetry class *mm*2, used for the theoretical development.

Table 1
Actual crystal dimensions.

$|\mathbf{n}|$ is the distance from the center of the crystal to its outer faces. Crystal volumes are 0.00146 (9) mm^3 (H − Sq) and 0.00127 (8) mm^3 (D − Sq).

	$l(0)$ (μm)	$l(h)$ (μm)	$t(0)$ (μm)	$2h$ (μm)	$\lvert\mathbf{n}_{\{011\}}\rvert$ (μm)	$\lvert\mathbf{n}_{\{110\}}\rvert$ (μm)
H − Sq	200 (5)	50 (5)	150 (5)	130 (5)	49 (3)	65 (3)
D − Sq	180 (5)	30 (5)	150 (5)	130 (5)	49 (3)	59 (3)

Table 2
Triclinic refinement of the unit cells.

	a (Å)	b (Å)	c (Å)	α (°)	β (°)	γ (°)
H − Sq	6.1324 (4)	5.2737 (10)	6.1427 (7)	89.992 (13)	89.952 (7)	89.999 (11)
D − Sq	6.1480 (3)	5.2700 (7)	6.1626 (4)	89.991 (8)	89.932 (4)	90.007 (7)

$$y = \mathcal{N}_y \sum_{j=C,D} \sum_{i=A,B} \int_0^1 \mathrm{d}w\,(1-ws)^2 \int_{M_{i-j}[\zeta(w)]} \mathrm{d}y \int_{S_{i-j}[y,\zeta(w)]} \mathrm{d}x \times \left| G_h^{i-j}[u(w)|x,y] A_h^{i-j}[\mu_0(w)|x,y] \right|^2 \quad (4)$$

and

$$P_h^{(0)}(\Delta\theta_{oh}) = \mathcal{N}_p \sum_{j=C,D} \int_0^1 \mathrm{d}w \int_{M_j[\zeta(w)]} \mathrm{d}y\,(1-ws) \times \left| \sum_{i=A,B} \int_{S_{i-j}[y,\zeta(w)]} \mathrm{d}x\,(1-ws) G_h^{i-j}[u(w)|x,y] \times Q_h^{i-j}[\xi_0(w), \Delta\theta_{oh}, \Delta\theta_{oh}^0|x,y] A_h^{i-j}[\mu_0(w)|x,y] \right|^2 \quad (5)$$

with

$$\mathcal{N}_y = \tfrac{1}{3}[6 + 2rs - 3(r+s)]\zeta(0)$$
$$\mathcal{N}_p = \tfrac{1}{2}\xi_0(0)\mathcal{N}_y.$$

The crystals used in the present experiments were shaped as symmetric bipyramids, *cf.* Fig. 3(*a*). This particular case, corresponding to $r = 1$, is readily handled by the formulas outlined above.

3. Experimental

In order to experimentally assess the theory, a suitable crystal had to be found. A specimen with a well defined (naturally developed) crystal shape and a rectangular cross section was required. In addition, it should be perfect (or nearly perfect) and also low absorbing so that dynamical features could be studied. Finally, it should endure significant exposure to a synchrotron beam. Crystals of squaric acid [3,4-dihydroxy-3-cyclobutene-1,2-dione, $H_2C_4O_4$], space group $P2_1/m$, fulfil these requirements very well. Specimens of various sizes were obtained by slow evaporation from aqueous solution at slightly elevated temperatures (Semmingsen, 1973). The deuterated samples were prepared by repeated recrystallization from 99.5% D_2O. Two separate sessions of beamtime were granted at the Swiss–Norwegian beamline (SNBL) at the ESRF – the first dedicated to the hydrogen (H − Sq) version, the second to the deuterated (D − Sq) version.

A schematic representation of a squaric acid crystal is shown in Figs. 3(*a*) and 3(*b*). Both the investigated crystals are modeled having a morphology represented by the symmetry class *mmm*. Indices of limiting planes and the length parameters adequate for describing the crystals are indicated in the figure. The dimensions of the specimens used in the experiments are given in Table 1. The crystals should be rotated an angle $\psi = \psi_{\mathbf{h}}^0$ about the reciprocal-lattice vectors $\{\mathbf{h}\}$ with respect to the initial orientation for scattering in the vertical plane as calculated from the orientation matrices. The base plane of the bipyramidal crystal then coincides with the plane of diffraction spanned by $\mathbf{K}_o$ and $\mathbf{K}_h$, the wave vectors of the incoming and diffracted beams, *cf.* Fig. 3(*b*).

The crystals were mounted approximately along $\mathbf{b}^*$ on a short glass capillary. The measurements were conducted using the KM6-CH six-circle κ diffractometer[2] at SNBL. The theoretical resolution in the diffractometer angles is 0.0002° except in φ, where $\delta\varphi_{\text{instrument}} = 0.0004°$. The geometry of this goniometer and the procedure for angle calculations have previously been described (Thorkildsen *et al.*, 1999). The samples were located about 15 m from the double-crystal Si (111) monochromator. The general layout of the experimental set-up is shown in Fig. 4. The unfocused beam cross section at the sample position was approximately 0.5×0.5 mm. The beam divergences, including the contribution from the monochromator, are about 25 μrad both horizontally and vertically at $\lambda = 1.0$ Å. The energy resolution of the monochromatic beam is $\Delta\lambda/\lambda \approx 1.4 \times 10^{-4}$.

The perfection of the crystals was judged based on ω scans for different reflections. Examples for the 303 reflection at $\lambda = 0.6 \wedge 1.2$ Å are shown in Fig. 5 for both the H − Sq and D − Sq crystals. In general, the rocking curves are seen to be narrow and homogeneous with $\text{FWHM}_{\text{D-Sq}} < \text{FWHM}_{\text{H-Sq}}$. For the H − Sq crystal, an orientation matrix was obtained from centering of a total of 60 reflections, 20 reflections within $14.3 < 2\theta_{oh} < 80.8°$ and 40 reflections within $93.0 < 2\theta_{oh} < 136.3°$, in the scintillation detector (Cyberstar YAP) aperture.[3] For the D − Sq crystal, the orientation matrix was formed using 68 reflections within $69.4 < 2\theta_{oh} < 128.5°$. The resulting lattice parameters from a triclinic refinement are given in Table 2.

[2] KM6-CH is a trademark of KUMA Diffraction Ltd, Wroclaw, Poland.
[3] The horizontal and vertical aperture acceptances are both 0.6°.

The linearity of the counting chain was tested using a radioactive source and the detector was found to be linear up to $\sim 2 \times 10^5$ counts s^{-1} (Pattison, 1999). Any variation with energy was considered negligible for the actual wavelength range. The energy window of the detector was optimized to avoid higher harmonic contributions from the monochromator.

For both the H − Sq and the D − Sq crystal, four repeated ω scans for three strong reflections, 103, 303 and 400, and a weak reference reflection, $20\bar{3}$, were recorded at room temperature at seven different wavelengths (0.6–1.2 Å) in regular intervals of 0.1 Å. For a *strong* reflection, multiple-scattering effects are pronounced and a dynamical theory is called upon for the calculation of the integrated power. A *weak* reflection is 'extinction free', *i.e.* the associated integrated power is given by kinematical theory.

Table 3 contains calculated values of the actual structure factors for $\lambda = 1.0$ Å. They are obtained from the positional and thermal parameters given in Table 2 of Semmingsen (1973) and Table 1 of Semmingsen (1975) for the H − Sq and the D − Sq versions, respectively. The atomic form factors are taken from Waasmaier & Kirfel (1995) with anomalous-scattering corrections based on the program *FPRIME* (Cromer & Liberman, 1970; Cromer, 1995). The variation of the structure factors with wavelength for the range $\lambda \in (0.6, 1.2)$ Å, owing to anomalous scattering, is approximately 0.6% for the strong reflections and 0.2% for the weak $20\bar{3}$ reflection. Possible errors in the calculated structure factors are neglected in this work.

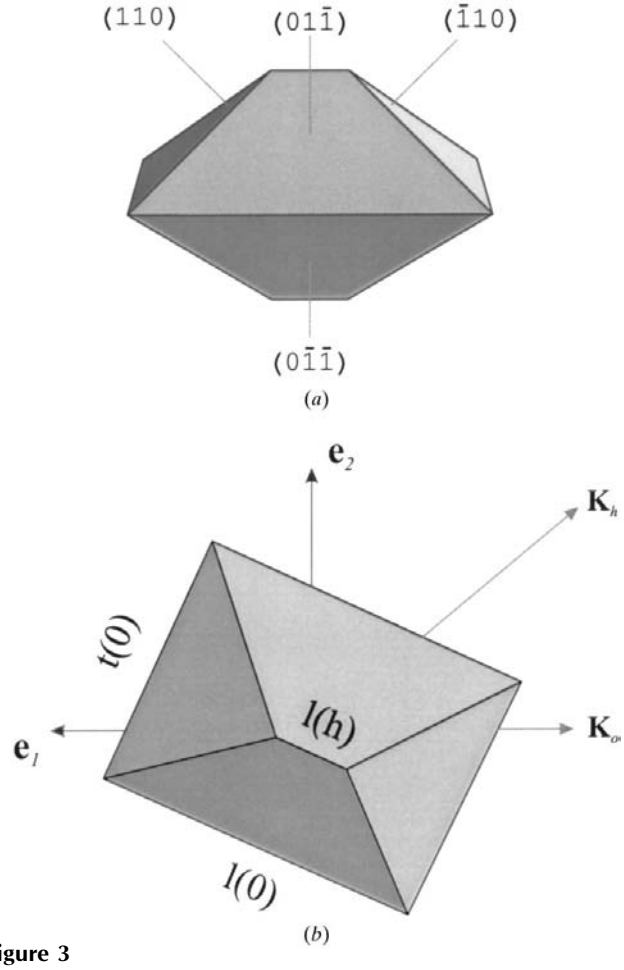

Figure 3
Actual crystal. (*a*) Indices of limiting planes. (*b*) Crystal orientation with (303) in scattering position. $\mathbf{e}_1$ points towards the incoming beam, ($\mathbf{e}_1$, $\mathbf{e}_2$) constitutes the reference vertical plane of the diffractometer, *cf.* Fig. 1 of Thorkildsen *et al.* (1999).

Table 3
The structure factors for the reflections used for experimental determination of generalized extinction factors.

Values calculated for $\lambda = 1.0$ Å. $|F_{000}|$ is included for completeness.

	$\lvert F_{000}\rvert$	$\lvert F_{103}\rvert$	$\lvert F_{303}\rvert$	$\lvert F_{400}\rvert$	$\lvert F_{20\bar{3}}\rvert$
H − Sq	116.2	22.81	28.41	27.51	0.7726
D − Sq	116.2	23.02	28.13	26.93	0.7384

The reflection 400 gives rise to *AB–AD* scattering, the other ones to *AB–CD* scattering. Every reflection was initially centered and the scans were performed using 400 steps of $2.5 \times 10^{-4\circ}$ over the profile using a counting time of 0.5 s $step^{-1}$ – ensuring adequate resolution and determination of the background level. In order not to saturate the detector,[4] different absorbers (Cu and Al foils) were used. Their attenuation factors were experimentally determined for each wavelength and each filter in question. The polarization coupling was checked throughout the entire wavelength interval by measuring high-angle reflections in both the horizontal and vertical planes.[5] Each reflection (and background range) was also assessed with regard to neighboring lattice nodes initiating multiple-beam diffraction.

During the experimental sessions, no crystal decay as a function of time was observed.

4. Analysis

The experimental determination of a generalized extinction factor is an indirect measurement that heavily relies on the idea of using a weak reflection to rescale the measured integrated powers of the strong reflections. Hence, wavelength-dependent terms that are not part of the physics of the scattering processes, but only related to the measuring apparatus and the state of the incoming X-ray beam, are eliminated.

The measured reflection profiles were integrated numerically using the *ListIntegrate* function (WolframResearch, 1999) of *Mathematica* (Wolfram, 1999). The end points of the integration, represented by step numbers $n = n_L \vee n_R$, were determined by individual inspection of plots of the mean power,

$$\overline{P}_{\mathbf{h}}(n) \stackrel{\text{def}}{=} (1/n) \sum_{i=1}^{n} P_{\mathbf{h}}(i),$$

[4] The maximum measured intensity was always kept below 1.5×10^5 counts s^{-1} – *i.e.* within the range of linear response of the detector.
[5] Accessible reflections in the horizontal plane are limited to $2\theta_{\text{horizontal}} < 45^\circ$ owing to mechanical constraints of the instrument.

where i counts the steps from the respective ends of the scan interval. n_L (n_R) was then associated with the beginning of the smooth positive slope of this function and the background calculated from $\overline{P}_{\mathbf{h}}(n_L)$ and $\overline{P}_{\mathbf{h}}(n_R)$. This was performed for each repetition of a scan and the average with its standard deviation was assigned to $\mathcal{P}_{\mathbf{h}}$, the net integrated diffracted power.

To obtain an estimate of the mosaic spread and possible crystal strains, the square of the FWHM of the rocking curves was plotted against $\tan^2\theta_{oh}$ according to the procedure outlined by Höche *et al.* (1986) and Coppens (1992):

$$\mathrm{FWHM}^2 = A^2 + B^2 \tan^2\theta_{oh}. \tag{6}$$

The parameter A is attributed to beam divergence and mosaic spread. B is mainly related to the relative wavelength spread, $\Delta\lambda/\lambda$, with additional contributions from the width of the intrinsic dynamical rocking curve and the variation in the lattice spacing owing to internal strains.

To determine values of the horizontal polarization fraction, f_h, we use the expression (Coppens, 1992)

$$f_h = \frac{(\mathcal{P}_v/\mathcal{P}_h) - \cos^2 2\theta_{oh}}{[1 + (\mathcal{P}_v/\mathcal{P}_h)](1 - \cos^2 2\theta_{oh})}. \tag{7}$$

$\mathcal{P}_v$ and $\mathcal{P}_h$ are integrated powers resulting from measurements of a weak reflection with the plane of diffraction aligned vertically and horizontally, respectively. The integrated powers are multiplied by the actual crystal transmission factors to correct for absorption owing to differences in the absolute crystal orientation in the two cases. To ensure maximum sensitivity, different reflections, *cf.* Table 4, were used for each wavelength by measuring as close as possible to the instrumental limit in the horizontal plane.

The theoretical expression for the integrated power for a strong reflection, $\mathbf{h}_1$, is

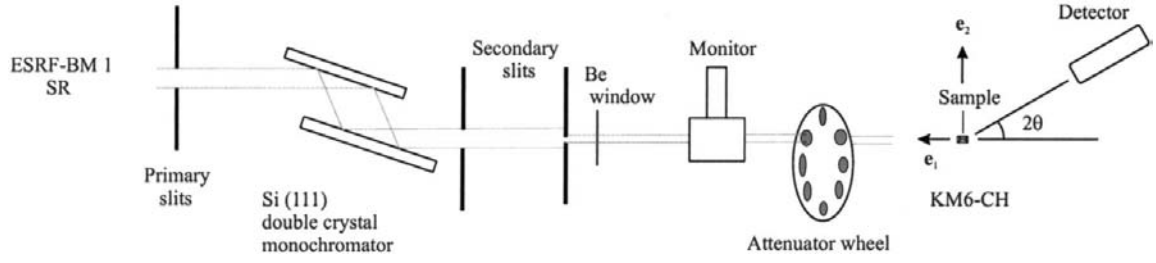

Figure 4
Schematic view of the experimental set-up.

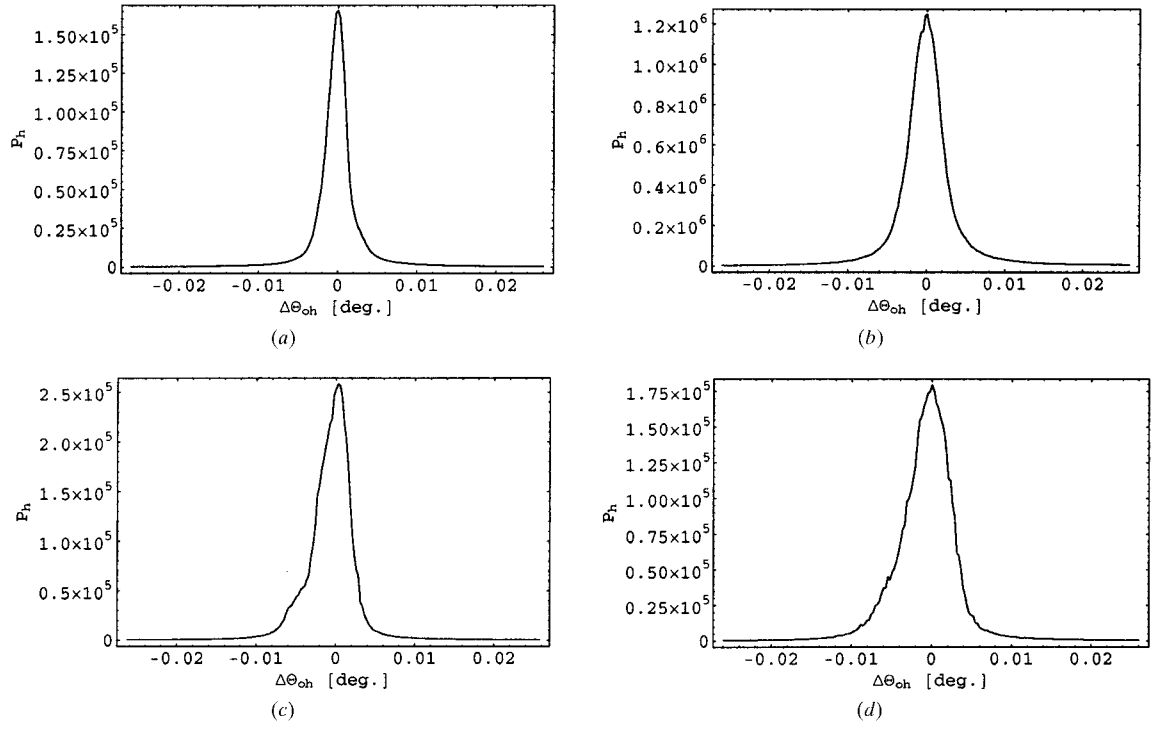

Figure 5
Measured rocking curves for the 303 reflection. (*a*) and (*b*) D − Sq at $\lambda = 0.6$ and 1.2 Å, respectively. (*c*) and (*d*) Measurements for H − Sq at the same wavelengths. (*a*) FWHM $= 2.7 \times 10^{-3\circ}$, (*b*) $4.4 \times 10^{-3\circ}$, (*c*) $4.4 \times 10^{-3\circ}$, (*d*) $6.0 \times 10^{-3\circ}$. Uncertainty: $\pm 0.1 \times 10^{-3\circ}$.

$$\mathcal{P}_{\mathbf{h}_1} = \frac{I_0(\lambda)}{A_f^*(\lambda)} J(\lambda) \frac{r_e^2 v}{V_c^2} \frac{|F_{\mathbf{h}_1}|^2 \lambda^3}{\sin 2\theta_{\mathbf{h}_1}} (1 + \alpha_{\mathbf{h}_1}) y. \quad (8)$$

A_f^* is the transmission factor of the attenuator foil. Thus, I_0/A_f^* is the intensity function of the incoming beam at the crystal. J is a scale function representing the performance of the detector. We assume that this function is independent of the intensity of the diffracted beam. $(1 + \alpha_{\mathbf{h}_1})$ is the correction factor for thermal diffuse scattering. It is calculated for the actual diffractometer geometry using a modified version of the procedure given by Stevens (1974). y is the generalized extinction factor that represents two-beam multiple-scattering effects along all possible optical routes in the crystal. For the strong reflections, polarization effects are also merged into y. The other terms in (8) have their usual interpretation: r_e is the classical electron radius, v the volume of the crystal, V_c the unit-cell volume, $|F_{\mathbf{h}_1}|$ the modulus of the structure factor and $\theta_{\mathbf{h}_1}$ the actual Bragg angle.[6]

For a weak reflection, $\mathbf{h}_2$, the corresponding expression becomes

$$\mathcal{P}_{\mathbf{h}_2} = I_0(\lambda) J(\lambda) \frac{r_e^2 v}{V_c^2} \frac{|F_{\mathbf{h}_2}|^2 \lambda^3}{\sin 2\theta_{\mathbf{h}_2}} p_{\mathbf{h}_2} (1 + \alpha_{\mathbf{h}_2}) A_{\mathbf{h}_2}. \quad (9)$$

This reflection is measured without use of any attenuator. According to our basic assumption, $J(\lambda)$ is the same as for the strong reflections. $p_{\mathbf{h}_2}$ is the polarization factor given by

$$p_{\mathbf{h}_2} = f_h + (1 - f_h) \cos^2 2\theta_{\mathbf{h}_2}, \quad (10)$$

while $A_{\mathbf{h}_2}$ is the absorption factor associated with single scattering events, *i.e.*

$$A_{\mathbf{h}_2} = (1/v) \int_v \mathrm{d}v \exp[-\mu(s_o + s_h)], \quad (11)$$

$s_o + s_h$ being the beam path measured along the incident and diffracted beams connecting the volume element dv to the entrance and exit surfaces. μ is the linear absorption coefficient. The absorption factors were calculated using the analytical approach by de Meulenaer & Tompa (1965).

For cases where TDS corrections are negligible, we obtain the following expression for the experimental generalized extinction factor:

$$y = y_{\exp} = \frac{\mathcal{P}_{\mathbf{h}_1} A_f^*}{\mathcal{P}_{\mathbf{h}_2}} \frac{\sin 2\theta_{\mathbf{h}_1}}{\sin 2\theta_{\mathbf{h}_2}} p_{\mathbf{h}_2} A_{\mathbf{h}_2} \frac{|F_{\mathbf{h}_2}|^2}{|F_{\mathbf{h}_1}|^2}. \quad (12)$$

The corresponding theoretical generalized extinction factor is calculated following equation (46) of Becker & Coppens (1974*a*):

$$y = y_{th} = f_h y_\perp + (1 - f_h) y_\parallel \cos^2 2\theta_{\mathbf{h}_1}, \quad (13)$$

where $y_\perp$ and $y_\parallel$ are calculated from (4) with $C = 1 \vee |\cos 2\theta_{\mathbf{h}_1}|$ in the expression for the coupling factor u, *cf.* equation (29).

[6] $\theta_{\mathbf{h}_1}$ represents a strong reflection and $\theta_{\mathbf{h}_2}$ the weak reflection. These symbols replace θ_{oh} whenever appropriate.

5. Results and discussion

The final rocking curves are represented by the average of four individual scans. The peak positions for each scan were internally consistent, indicating a good stability of the instrument. In order to assess the crystal quality, the measured

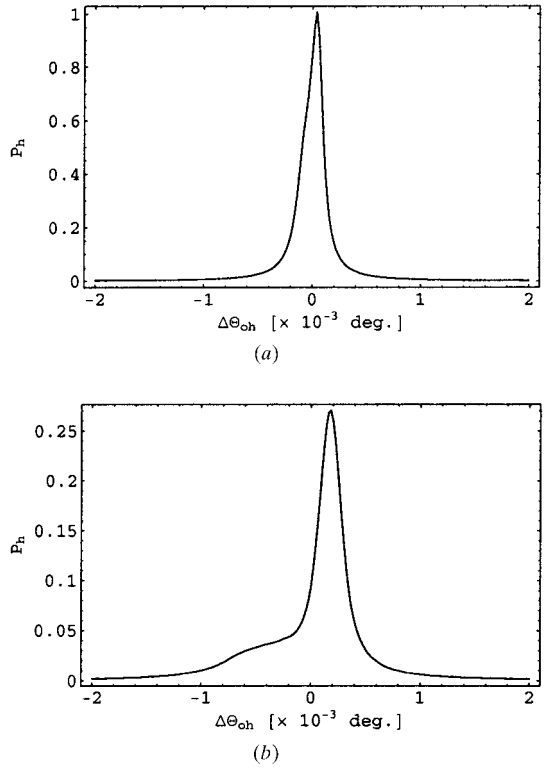

Figure 6
Theoretical rocking curves for the 303 reflection in D − Sq. (*a*) $\lambda = 0.6$ Å and (*b*) $\lambda = 1.2$ Å. (*a*) FWHM $= 2.1 \times 10^{-4\circ}$, (*b*) $2.6 \times 10^{-4\circ}$. The apparent tail in (*b*) is caused by refraction effects. There are different shifts in $\Delta\theta_{oh}$ with respect to zero in the contributions to the rocking curve from the various scattering processes. These shifts are, according to equations (24)–(27), $(\Delta\theta_{oh}^0/2)(1 - \beta_+/\beta_-)$ and $(\Delta\theta_{oh}^0/2)(1 - \delta_+/\delta_-)$, respectively. For case (*a*), we have $0.46 \times 10^{-4\circ}$ and $-0.71 \times 10^{-4\circ}$ and, for case (*b*), $1.8 \times 10^{-4\circ}$ and $-4.7 \times 10^{-4\circ}$. Thus with increasing wavelength these shifts are being resolved in the rocking curve.

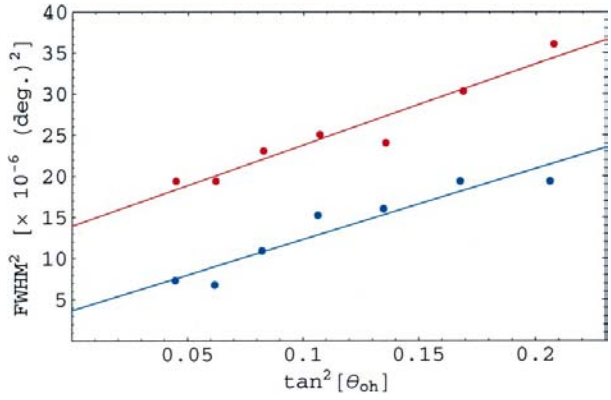

Figure 7
FWHM^2 as function of $\tan^2\theta_{oh}$. Red line (points) represents H − Sq. Blue line (points) represents D − Sq.

rocking curves (Fig. 5) should be compared to those theoretically calculated for the same geometry (Fig. 6). These represent the intrinsic dynamical contribution, and it is seen that the FWHM's ($\Delta_{\rm dyn}$) are about $2 \times 10^{-4\circ}$. Owing to refraction effects within the finite crystal, the intrinsic dynamical width, as a function of λ, will not have a simple $\tan\theta_{oh}$ dependence. However, since $\Delta_{\rm dyn} \ll \Delta\lambda/\lambda$, this will not preclude the use of (6). The main contributions to the widths of the measured profiles thus originate from instrumental broadening, wavelength dispersion and crystal imperfection ('mosaicity'), and are assigned from plots of FWHM^2 *vs* $\tan^2\theta_{oh}$. An example of such a plot for the H − Sq and D − Sq 303 reflection is given in Fig. 7. The least-squares-fitted lines shown in this figure give $\Delta\lambda/\lambda = 1.6\,(1) \times 10^{-4}$ for D − Sq and $1.7\,(1) \times 10^{-4}$ for H − Sq. For the whole set of measured reflections, we have $\Delta\lambda/\lambda \in (1.6, 2.0) \times 10^{-4}$. Compared with the expected result of 1.4×10^{-4} for this beamline, this may indicate minor contributions from internal strains. There is however no indication in the experiments of excess strain in H − Sq *vs* D − Sq. Based on the measurements of the 303 reflection, we obtain a FWHM of the mosaic distribution function, $\Delta_{\rm mos} = 1.3\,(7) \times 10^{-3\circ}$ for D − Sq and $\Delta_{\rm mos} = 3.4\,(3) \times 10^{-3\circ}$ for H − Sq. These values are representative of the measurements of the 103 and 400 reflections as well. Hence, we conclude that neither of the two crystals used is perfect in the strict sense but the deuterated specimen clearly exhibits a lower degree of 'mosaicity'.

In order to scale the data, the weak reflection $20\bar{3}$ was chosen. ω rocking curves of this reflection for the two crystals at $\lambda = 0.6$ Å are depicted in Fig. 8.

The use of a weak reflection for scaling purposes demands that three-beam *Umweganregung* scattering is not present. Otherwise large perturbations of the diffracted two-beam power may occur. This was carefully examined using the

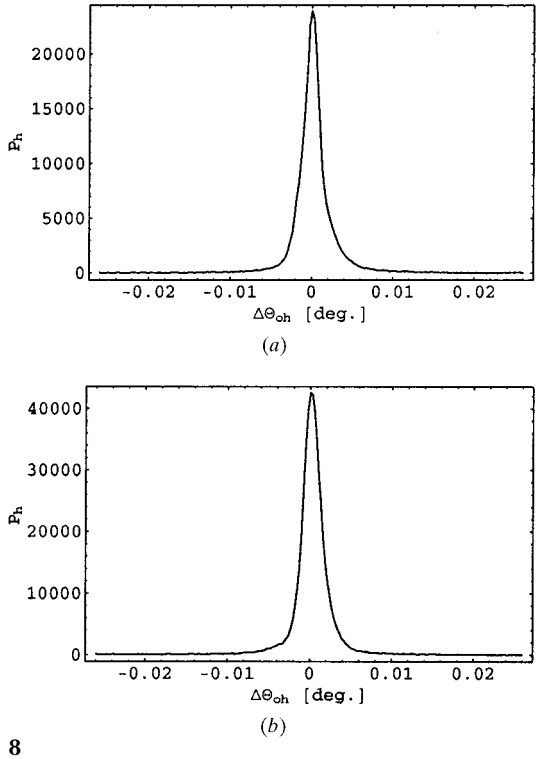

Figure 8
Measured rocking curves of the weak $20\bar{3}$ reflection. (*a*) D − Sq and (*b*) H − Sq. $\lambda = 0.6$ Å. (*a*) FWHM $= 2.2 \times 10^{-3\circ}$, (*b*) $2.4 \times 10^{-3\circ}$.

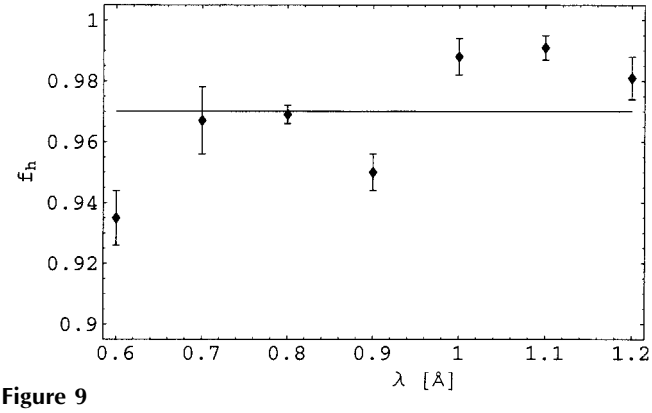

Figure 9
Polarization measurements. Determination of the horizontal polarization fraction f_h as a function of wavelength. Measurements for H − Sq. The horizontal line represents the average value used in the calculations.

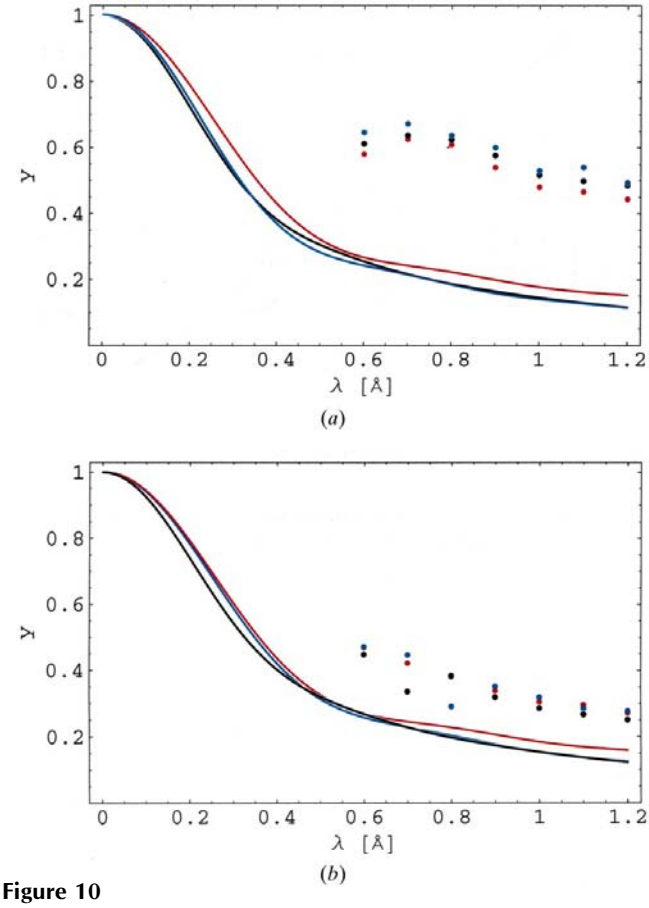

Figure 10
Generalized extinction factors – theoretical and experimental. (*a*) H − Sq and (*b*) D − Sq. Blue line (points) represents reflection 103. Black line (points) represents reflection 303. Red line (points) represents reflection 400.

Table 4
Data for assigning the state of polarization of the beam.

Measurements for H − Sq. Different attenuator foils were used for different wavelengths.

λ (Å)	0.6	0.7	0.8	0.9	1.0	1.1	1.2
hkl	$(5\bar{3}4)$	$(4\bar{4}2)$	$(5\bar{2}2)$	$(2\bar{3}3)$	$(0\bar{3}3)$	$(0\bar{1}4)$	$(3\bar{1}2)$
F_{hkl}	6.23	4.33	5.71	5.92	2.59	1.17	1.66
$\mathcal{P}_v$	195.2 (11)	133.5 (13)	451.3 (15)	542 (3)	80.0 (6)	86.6 (2)	276.6 (12)
$\mathcal{P}_h$	117.9 (11)	74.3 (7)	236.7 (8)	309.0 (15)	42.1 (2)	45.8 (2)	149.8 (13)

Table 5
Absorption coefficient, μ, absorption factor, $A_{\mathbf{h}_2}$, and polarization factor, $p_{\mathbf{h}_2}$, for the weak reflection $\mathbf{h}_2 = 20\bar{3}$, as calculated for the actual wavelengths, λ.

λ (Å)		0.6	0.7	0.8	0.9	1.0	1.1	1.2
μ (cm^{-1})		0.7189	1.180	1.811	2.639	3.693	5.000	6.591
$A_{20\bar{3}}$	D − Sq	0.9915 (5)	0.9861 (8)	0.9787 (12)	0.969 (2)	0.957 (2)	0.942 (3)	0.925 (3)
	H − Sq	0.9913 (5)	0.9858 (8)	0.9783 (12)	0.968 (2)	0.956 (2)	0.941 (3)	0.924 (3)
$p_{20\bar{3}}$	D − Sq	0.993 (2)	0.990 (3)	0.988 (4)	0.985 (5)	0.981 (6)	0.978 (7)	0.974 (9)
	H − Sq	0.9964 (12)	0.995 (2)	0.994 (2)	0.992 (3)	0.991 (3)	0.989 (4)	0.987 (4)

Table 6
Observed integrated powers for deuterated squaric acid.

λ (Å)	0.6	0.7	0.8	0.9	1.0	1.1	1.2
$\mathcal{P}_{103}A_f^*$ (×10^4)	0.99 (3)	1.41 (3)	1.37 (6)	3.01 (14)	5.7 (2)	12.7 (4)	28.5 (8)
$\mathcal{P}_{303}A_f^*$ (×10^4)	1.06 (3)	1.20 (2)	2.06 (7)	3.13 (14)	5.9 (2)	13.8 (5)	30.3 (9)
$\mathcal{P}_{400}A_f^*$ (×10^4)	1.07 (3)	1.45 (3)	1.97 (8)	3.18 (14)	6.0 (2)	14.6 (5)	31.2 (9)
$\mathcal{P}_{20\bar{3}}$	18.85 (10)	28.12 (12)	41.7 (3)	74.84 (11)	153.8 (3)	376.4 (10)	854 (2)

Table 7
Observed integrated powers for squaric acid.

λ (Å)	0.6	0.7	0.8	0.9	1.0	1.1	1.2
$\mathcal{P}_{103}A_f^*$ (×10^4)	2.13 (6)	2.40 (6)	3.33 (10)	3.62 (9)	3.65 (11)	4.23 (14)	4.44 (13)
$\mathcal{P}_{303}A_f^*$ (×10^4)	2.36 (9)	2.67 (7)	3.85 (12)	4.12 (10)	4.25 (13)	4.7 (2)	5.3 (2)
$\mathcal{P}_{400}A_f^*$ (×10^4)	2.21 (6)	2.59 (6)	3.70 (12)	3.8 (2)	3.88 (12)	4.31 (15)	4.74 (14)
$\mathcal{P}_{20\bar{3}}$	33.1 (3)	35.6 (3)	51.7 (12)	59.0 (6)	66.5 (11)	74.4 (3)	83.9 (2)

procedure of Tanaka & Saito (1975) adapted to the actual diffractometer geometry. Three-beam cases that might have introduced systematic errors in the observed integrated powers were not found. The same is true for the strong reflections as well, where *Aufhellung* cases might have caused a reduction of the integrated power with respect to the true two-beam level.

The results from the absorption analysis of the weak reflection are summarized in Table 5. At $\lambda = 1.0$ Å, the function $A_{20\bar{3}}(\psi)$ for D − Sq shows a smooth harmonic variation within (0.957,0.973). Maximum absorption occurs for $\psi = \psi^0_{20\bar{3}}$ giving an orientation with the base plane of the bipyramidal crystal parallel to the plane of diffraction. The value of the absorption factor for this orientation is identical to what we calculate from (4) by replacing the Green functions with unity (*i.e.* for $u = 0$). Simulations indicate that uncertainties in the dimensions of the crystals lead to errors in the absorption factor $A_{20\bar{3}}$ of less than 0.4%. It is to be noticed that, in the measurements with the H − Sq crystal, there is a misalignment in ψ of approximately 20° from the 'ideal' scattering situation as depicted in Fig. 3(*b*), since the final rotation $\psi^0_{\mathbf{h}}$ about **h** was not executed at this experimental session. The absorption factors given in Table 5 refer to the actual angle settings.

Measurements of a set of reflections in the horizontal and vertical modes (Table 4) yielded the horizontal polarization fraction as a function of wavelength, *cf.* Fig. 9. We used the average values, 0.97 (1) for H − Sq and 0.94 (2) for D − Sq, as estimates for f_h when calculating the polarization factor for the weak reflection. The results of this calculation are included in Table 5. The standard deviation associated with f_h causes an uncertainty in $p_{20\bar{3}}$ that increases with wavelength. Maximum relative error amounts to 0.5 and 0.9% for H − Sq and D − Sq, respectively.

The correction factors for TDS (one- and two-phonon scattering) were calculated using the elastic constants of squaric acid (Rehwald & Vonlanthen, 1978; Semmingsen *et al.*, 1995). Since only low-angle reflections were involved together with a very narrow scan range in ω and small detector slits, the corrections amounted to less than 0.1%, *e.g.* $\alpha_{400} = 3.3 \times 10^{-4}$ to $\alpha_{303} = 9.7 \times 10^{-4}$ in H − Sq for $\lambda = 1.0$ Å. The variations for the actual range of wavelengths were negligible.

Tables 6 and 7 sum up the experimentally obtained diffracted powers. In fact, the largest contribution to the quoted uncertainties originates from the estimated errors in the transmission factors of the attenuator foils (A_f^* is in the range 10–6600). Using (12), we were able to deduce the generalized extinction factors as a function of wavelength for the three strong reflections. The results are summarized in Fig. 10 along with the theoretically calculated curves, *cf.* equation (13). The relative errors in the experimentally determined values for y are in the range 2–5%, while the relative errors in theoretical values, owing to uncertainties in crystal dimension and state of polarization, are less than 1%. The precision of the measurements is good, except from two outliers for D − Sq at wavelengths of 0.7 and 0.8 Å. The reason for this is a slight off-centering (in 2θ and $\varphi + \omega$, respectively – not realised at the time of measurements) of

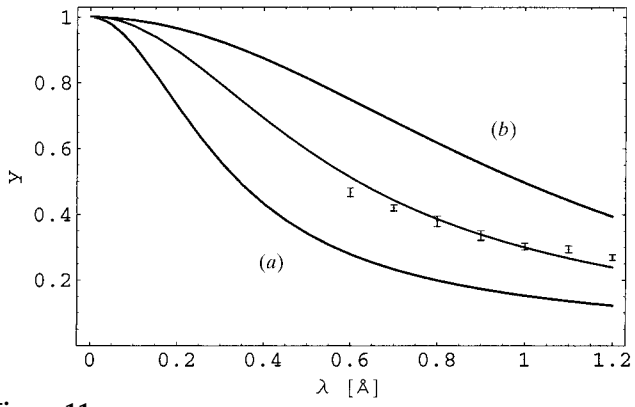

Figure 11
Theoretical results for the generalized extinction factor for the 400 reflection in D − Sq for the π-polarization component ($C = 1$) based upon the Becker–Coppens theory. (*a*) Product of primary-extinction factor, ordinary absorption factor and polarization factor. (*b*) Product of secondary-extinction factor, ordinary absorption factor and polarization factor. Actual measurements are included together with the best fit (line).

these two reflections. Otherwise, the sets of three values for $y_{\rm exp}$ for D − Sq exhibit less spread than the corresponding sets for H − Sq. The internal spread within a set for D − Sq is comparable to what is found for $y_{\rm calc}$. For H − Sq, the experimental values have a fixed order, $y_{400} < y_{303} < y_{103}$, contrary to the theoretical predictions. We find no straightforward explanation of this feature apart from possible effects owing to the misalignment in ψ.

The experimentally determined generalized extinction factors are generally shifted towards higher values than predicted from the theory. This must in part be due to the mosaicity present in the crystals giving rise to incoherently scattered waves and in part due to the instrumental resolution. The degree of imperfection is seen to be larger in H − Sq than in D − Sq.

Finally, Fig. 11 gives the theoretical generalized extinction factors[7] as calculated for the $\mathbf{h}_1 = 400$ reflection in D − Sq using the Becker–Coppens formalism (Becker & Coppens, 1974*a*). Fig. 11(*a*) represents the product $y_p \times A_s(\mu r, \theta_{\mathbf{h}_1}) p_{\mathbf{h}_1}$, where y_p is the primary-extinction factor for a perfect sphere (domain) of radius r, A_s is the ordinary absorption factor for a sphere as calculated from Thorkildsen & Larsen (1998*b*) and p is the polarization factor from (10). Fig. 11(*b*) represents the product $y_s \times A_s(\mu R, \theta_{\mathbf{h}_1}) p_{\mathbf{h}_1}$, where y_s is the secondary-extinction factor (type I crystal, Gaussian distribution) and R is the radius of the spherical model crystal. For the simulations shown in the figure, we have $r = R = 67$ µm, giving an identical value for the crystal volume, as quoted for the actual bipyramidal crystal. The value $\Delta_{\rm mos} = 1.0 \times 10^{-3\circ}$ is chosen for the mosaic spread. The relative error of Fig. 11(*a*) compared to the simulation based on (4) is less than 20% for the actual reflection. The results of the measurements are also included in the figure. When fitting these observations to a combined expression, $y_p y_s \times A_s(\mu R, \theta_{\mathbf{h}_1}) p_{\mathbf{h}_1}$, the best result is obtained for negligible secondary extinction and with y_p calculated for $r = 37$ µm.

[7] Only a single state of polarization, $C = 1$, is considered here.

6. Concluding remarks

This work combines theory and experiments to address questions related to generalized extinction in a finite crystal. In this context, squaric acid seems to be a very good model system for these kinds of studies. The use of a weak reflection for scaling purposes has proved to be a successful method in obtaining the generalized extinction factors.

The structure factors, *cf.* Table 3, were calculated using the independent-atom model (Coppens, 1997). A crucial point is whether this model gives accurate values for the reflections used in the present measurements. Otherwise, large systematic errors in the extracted values for the generalized extinction factor may occur when applying equation (12). A recent work (Noda, 2000) gives very good agreement between $|F_{\rm obs}(h0l)|$ and $|F_{\rm calc}(h0l)|$ for both H − Sq and D − Sq. However, accurate charge-density studies based on synchrotron-radiation data, for both crystal types, are called for before this issue may be finally settled.

It is evident from the present experimental results that even for nearly perfect crystals the theory should be extended to include effects owing to imperfections. This could be pursued by generalizing the Takagi–Taupin equations in the following two ways: Either by modeling the exact displacement field (based for instance on topographical information) or by using the more general concepts offered by the so-called statistical dynamical theory (Kato, 1980; Becker & Al Haddad, 1990, 1992; Guigay, 1989). This extension seems to be vital, *e.g.* in accurate charge-density studies, if the current method is to be used to give estimates of relevant parameters that determine the amount of extinction in a mosaic crystal.

APPENDIX *A*
Definitions

The geometrical parameters $\delta_\pm$ and $\beta_\pm$for *AB–CD* scattering are defined by[8]

$$\beta_\pm = \frac{\sin\theta_{oh}}{\sin(\gamma \pm \theta_{oh})} \tag{14}$$

$$\delta_\pm = \frac{\cos\theta_{oh}}{\cos(\gamma \pm \theta_{oh})}. \tag{15}$$

The boundary-value Green functions for the actual combinations of positions for source and exit points are

$$G_h^{A-C}(u|x,y) = J_0(2\{u[2\beta_+ - (\beta_+/\beta_-)x]x\}^{1/2}) \tag{16}$$

$$G_h^{A-D}(u|x,y) = J_0(2\{u[2\beta_+\delta_- y - (\beta_+/\beta_-)x]x\}^{1/2}) \tag{17}$$

$$G_h^{B-C}(u|x,y) = J_0(2\{u[2\beta_-\delta_+ y - (\delta_+/\delta_-)x]x\}^{1/2}) \tag{18}$$

$$G_h^{B-D}(u|x,y) = J_0(2\{u[2\zeta\delta_+ - (\delta_+/\delta_-)x]x\}^{1/2}). \tag{19}$$

[8] For the allowed ranges of θ_{oh} and γ, the parameters are always positive. Notice the change from the definition given for *AB–AD* scattering [equations (9) and (10) of TL99*a*].

Table 8
Integration ranges in x and y for $\zeta \leq \beta_+/\delta_+$.

$i-j$	$M_{i-j}(\zeta)$	$S_{i-j}(y,\zeta)$
$A-D$	$(0, \zeta/\beta_-)$	$(0, 2\beta_-\delta_- y)$
	$(\zeta/\beta_-, \zeta\delta_+/\beta_+\delta_-)$	$(0, \zeta/\beta_+ - [\delta_-/\delta_+]y)$
$B-C$	$(0, \zeta/\beta_-)$	$(0, 2\beta_-\delta_- y)$
$B-D$	$(\zeta/\beta_-, \zeta\delta_+/\beta_+\delta_-)$	$(\zeta/\beta_+ - [\delta_-/\delta_+]y, 2\zeta\delta_-)$
	$(\zeta\delta_+/\beta_+\delta_-, 1/\delta_-)$	$(0, 2\zeta\delta_-)$

Table 9
Integration ranges in x and y for $\beta_+/\delta_+ \leq \zeta \leq \beta_-/\delta_-$.

$i-j$	$M_{i-j}(\zeta)$	$S_{i-j}(y,\zeta)$
$A-C$	$(\beta_+/\beta_-\delta_+, \zeta/\beta_-)$	$(0, [\beta_-/\beta_+]y - 1/\delta_+)$
$A-D$	$(0, \zeta/\beta_-)$	$(0, 2\beta_-\delta_- y)$
	$(\zeta/\beta_-, 1/\delta_-)$	$(0, \zeta/\beta_+ - [\delta_-/\delta_+]y)$
$B-C$	$(0, \beta_+/\beta_-\delta_+)$	$(0, 2\beta_-\delta_- y)$
	$(\beta_+/\beta_-\delta_+, \zeta/\beta_-)$	$([\beta_-/\beta_+]y - 1/\delta_+, 2\beta_-\delta_- y)$
$B-D$	$(\zeta/\beta_-, 1/\delta_-)$	$(\zeta/\beta_+ - [\delta_-/\delta_+]y, 2\zeta\delta_-)$

The factors related to absorption are

$$A_h^{A-C}(\mu_0|x,y) = \exp(-[\mu_0/2]\{2\beta_+ + [1-(\beta_+/\beta_-)]x\}) \quad (20)$$

$$A_h^{A-D}(\mu_0|x,y) = \exp(-[\mu_0/2]\{2\beta_+\delta_- y + [1-(\beta_+/\beta_-)]x\}) \quad (21)$$

$$A_h^{B-C}(\mu_0|x,y) = \exp(-[\mu_0/2]\{2\beta_-\delta_+ y + [1-(\delta_+/\delta_-)]x\}) \quad (22)$$

$$A_h^{B-D}(\mu_0|x,y) = \exp(-[\mu_0/2]\{2\zeta\delta_+ + [1-(\delta_+/\delta_-)]x\}). \quad (23)$$

The phase factors associated with each scattering process become, *cf.* equations (11)–(14) of TL99*b*,

$$Q_h^{A-C}(\xi_0, \Delta\theta_{oh}, \Delta\theta_{oh}^0|x,y) = \exp(-\pi i\xi_0\Delta\theta_{oh}x)\exp\left(\pi i\xi_0(\Delta\theta_{oh}^0/2) \times \{2\beta_+ + [1-(\beta_+/\beta_-)]x\}\right) \quad (24)$$

$$Q_h^{A-D}(\xi_0, \Delta\theta_{oh}, \Delta\theta_{oh}^0|x,y) = \exp(-\pi i\xi_0\Delta\theta_{oh}x)\exp\left(\pi i\xi_0(\Delta\theta_{oh}^0/2) \times \{2\beta_+\delta_- y + [1-(\beta_+/\beta_-)]x\}\right) \quad (25)$$

$$Q_h^{B-C}(\xi_0, \Delta\theta_{oh}, \Delta\theta_{oh}^0|x,y) = \exp(-\pi i\xi_0\Delta\theta_{oh}x)\exp\left(\pi i\xi_0(\Delta\theta_{oh}^0/2) \times \{2\beta_-\delta_+ y + [1-(\delta_+/\delta_-)]x\}\right) \quad (26)$$

$$Q_h^{B-D}(\xi_0, \Delta\theta_{oh}, \Delta\theta_{oh}^0|x,y) = \exp(-\pi i\xi_0\Delta\theta_{oh}x)\exp\left(\pi i\xi_0(\Delta\theta_{oh}^0/2) \times \{2\zeta\delta_+ + [1-(\delta_+/\delta_-)]x\}\right). \quad (27)$$

The definitions of the basic parameters of the theory are summarized below, *cf.* Appendix *A* of TL99*b*:

$$\zeta = (t/l)\tan\theta_{oh} \quad (28)$$

$$u = (r_e\lambda C/V_c)^2 F_{\mathbf{h}}F_{\bar{\mathbf{h}}}(l/2\sin\theta_{oh})^2 \quad (29)$$

$$\mu_0 = \mu(l/2\sin\theta_{oh}) \quad (30)$$

$$\xi_0 = (2l/\lambda)\cos\theta_{oh} \quad (31)$$

$$\Delta\theta_{oh}^0 = -(r_e\lambda^2/\pi V_c)\Re F_0/\sin 2\theta_{oh}. \quad (32)$$

APPENDIX *B*
Integration set-up

The integration set-up for the calculation of the generalized extinction factor for *AB–CD* scattering is summarized in Tables 8–10. As was the case for *AB–AD* scattering, the integration limits depend upon the value of the parameter ζ.

Table 10
Integration ranges in x and y for $\zeta \geq \beta_-/\delta_-$.

$i-j$	$M_{i-j}(\zeta)$	$S_{i-j}(y,\zeta)$
$A-C$	$(\beta_+/\beta_-\delta_+, 1/\delta_-)$	$(0, [\beta_-/\beta_+]y - 1/\delta_+)$
	$(1/\delta_-, \zeta/\beta_-)$	$(0, 2\beta_-)$
$A-D$	$(0, 1/\delta_-)$	$(0, 2\beta_-\delta_- y)$
$B-C$	$(0, \beta_+/\beta_-\delta_+)$	$(0, 2\beta_-\delta_- y)$
	$(\beta_+/\beta_-\delta_+, 1/\delta_-)$	$([\beta_-/\beta_+]y - 1/\delta_+, 2\beta_-\delta_- y)$

We acknowledge the contribution by Professor Y. Noda for communicating some of his results prior to publication. Furthermore, stimulating discussions with Drs P. Pattison and R. H. Mathiesen are appreciated. Finally, we thank Dr T. Gustafsson for providing the source code for calculation of the TDS corrections.

The measurements were carried out at SNBL, ESRF, Experiments 01-02-173, 01-02-244. We gratefully acknowledge the support from the SNBL staff. This work has been supported by Norges Forskningsråd, Grants 129638/431 and 138660/431.

References

Becker, P. & Al Haddad, M. (1990). *Acta Cryst.* A**46**, 123–129.
Becker, P. & Al Haddad, M. (1992). *Acta Cryst.* A**48**, 121–134.
Becker, P. & Coppens, P. (1974*a*). *Acta Cryst.* A**30**, 129–147.
Becker, P. & Coppens, P. (1974*b*). *Acta Cryst.* A**30**, 148–153.
Becker, P. & Coppens, P. (1975). *Acta Cryst.* A**31**, 417–425.
Becker, P. & Dunstetter, F. (1984). *Acta Cryst.* A**40**, 241–251.
Cooper, M. J. (1979). *Acta Cryst.* A**35**, 176–180.
Cooper, M. J. & Rouse, K. D. (1976). *Acta Cryst.* A**32**, 806–812.
Coppens, P. (1992). *Synchrotron Radiation Crystallography*. New York: Academic Press.
Coppens, P. (1997). *X-ray Charge Densities and Chemical Bonding*. Oxford University Press.
Cromer, D. (1995). Private communication.
Cromer, D. & Liberman, D. (1970). *J. Chem. Phys.* **53**, 1891–1898.
Graafsma, H., Souhassou, M., Puig-Molina, A., Harkema, S., Kvick, Å. & Lecomte, C. (1998). *Acta Cryst.* B**54**, 193–195.
Guigay, J. P. (1989). *Acta Cryst.* A**45**, 241–244.
Hester, J. R. & Okamura, F. P. (1996). *Acta Cryst.* A**52**, 700–704.
Höche, H. R., Schulz, H., Weber, H. P., Belzner, A., Wolf, A. & Wulf, R. (1986). *Acta Cryst.* A**42**, 106–110.
Kato, N. (1980). *Acta Cryst.* A**36**, 171–177.
Lippmann, T. & Schneider, J. R. (2000). *J. Appl. Cryst.* **33**, 156–167.
Mathieson, A. M. (1977). *Acta Cryst.* A**33**, 133–136.
Mathieson, A. M. (1979). *Acta Cryst.* A**35**, 50–57.
Meulenaer, J. de & Tompa, H. (1965). *Acta Cryst.* **19**, 1014–1018.

Niimura, N., Tomiyoshi, S., Takahashi, J. & Harada, J. (1975). *J. Appl. Cryst.* **8**, 560–561.
Noda, Y. (2000). Private communication.
Palmer, A. & Jauch, W. (1995). *Acta Cryst.* A**51**, 662–667.
Pattison, P. (1999). Private communication.
Rehwald, W. & Vonlanthen, A. (1978). *Phys. Status Solidi B*, **90**, 61–66.
Schneider, J. R. (1977). *Acta Cryst.* A**33**, 235–243.
Semmingsen, D. (1973). *Acta Chem. Scand.* **27**, 3961–3972.
Semmingsen, D. (1975). *Acta Chem. Scand.* A**29**, 470–473.
Semmingsen, D., Tun, Z., Nelmes, R. J., McMullan, R. K. & Koetzle, T. F. (1995). *Z. Kristallogr.* **210**, 934–947.
Stevens, E. D. (1974). *Acta Cryst.* A**30**, 184–189.
Stevenson, A. W. & Barnea, Z. (1983). *Acta Cryst.* A**39**, 538–547.
Suortti, P. (1982*a*). *Acta Cryst.* A**38**, 642–647.
Suortti, P. (1982*b*). *Acta Cryst.* A**38**, 648–656.
Takagi, S. (1962). *Acta Cryst.* **15**, 1311–1312.
Takagi, S. (1969). *J. Phys. Soc. Jpn*, **26**, 1239–1253.
Tanaka, K. & Saito, Y. (1975). *Acta Cryst.* A**31**, 841–845.
Taupin, D. (1964). *Bull. Soc. Fr. Minéral. Cristallogr.* **87**, 469–511.
Thorkildsen, G. & Larsen, H. B. (1998*a*). *Acta Cryst.* A**54**, 172–185.
Thorkildsen, G. & Larsen, H. B. (1998*b*). *Acta Cryst.* A**54**, 186–190.
Thorkildsen, G. & Larsen, H. B. (1998*c*). *Acta Cryst.* A**54**, 416–429.
Thorkildsen, G. & Larsen, H. B. (1999*a*). *Acta Cryst.* A**55**, 1–13.
Thorkildsen, G. & Larsen, H. B. (1999*b*). *Acta Cryst.* A**55**, 840–854.
Thorkildsen, G., Mathiesen, R. H. & Larsen, H. B. (1999). *J. Appl. Cryst.* **32**, 943–950.
Waasmaier, D. & Kirfel, A. (1995). *Acta Cryst.* A**51**, 416–431.
Wolfram, S. (1999). *The Mathematica Book*, 4th ed. Champain, IL 61820, USA: Wolfram Media/Cambridge University Press.
WolframResearch (1999). *Mathematica 4.0 Standard Add-on Packages.* Champain, IL 61820, USA: Wolfram Media.
Zachariasen, W. H. (1967). *Acta Cryst.* **23**, 558–564.